

**Self-focusing dynamics of ultraintense accelerating Airy waveforms in water**Craig Ament, Miroslav Kolesik, Jerome V. Moloney, and Pavel Polynkin\*  
*College of Optical Sciences, The University of Arizona, Tucson, Arizona 85721, USA*

(Received 12 August 2012; published 31 October 2012)

We report experiments and numerical simulations on the self-focusing and filamentation of ultraintense femtosecond Airy waveforms in water. The accelerating property of Airy waveforms results in the generation of distinct features in the angularly resolved spectra of forward-propagating supercontinuum emission. Fitting these features with appropriate phase-matching conditions allows for the quantification of the propagation history of the waveforms.

DOI: [10.1103/PhysRevA.86.043842](https://doi.org/10.1103/PhysRevA.86.043842)

PACS number(s): 42.65.Jx, 42.65.Ky, 42.65.Tg, 42.65.Re

Studies of the self-action effects involved in the propagation of ultraintense and ultrashort laser pulses in various transparent media are a research area receiving significant contemporary interest. These studies can be conceptually divided into two broad classes: those on propagation in gaseous media such as common air and those on propagation in condensed media such as transparent liquids and solids. According to the conventional paradigm, when a high-peak-power laser pulse propagates in a transparent gas, Kerr self-focusing is balanced, in a dynamic way, by the beam diffraction and the defocusing effect of plasma generated on the beam axis via multiphoton ionization [1–3]. It has recently been suggested that the above filamentation scenario needs to be reconsidered with the inclusion of higher order defocusing terms in the instantaneous Kerr response of the propagation medium [4]. These new terms become operative at a sufficiently high optical intensity and stabilize filament propagation without the need for the defocusing action from plasma. The debate on the validity of this new filamentation paradigm is ongoing at the time of writing. In either of the two filamentation scenarios, the competition among various participating focusing and defocusing effects results in the generation of extended plasma channels or filaments that have various technologically important properties and may have practical utility. Transparent condensed media offer a convenient platform for experimental studies of filament formation, as the critical power for self-focusing is lower by three orders of magnitude than that in a gas under normal conditions.

Although filamentations of ultraintense laser pulses in gaseous and condensed media bear certain similarities, the two cases are significantly different. In a gas, the dispersion of the medium cannot be completely ignored, but it does not play the dominant role in the stabilization of self-focusing. In a condensed medium, the material dispersion becomes the major player in the propagation dynamics. The laser pulse is typically split into subpulses upon propagation. The temporal pulse splitting arrests the self-focusing collapse to a singularity in this case [5]. Although plasma is generated through multiphoton ionization in condensed media, its effect in stabilizing filament propagation is secondary to that of dispersion, except for cases where the peak power of the laser pulse significantly exceeds the threshold power for self-focusing [6].

The overwhelming majority of prior studies on pulse-splitting dynamics and other phenomena associated with laser filamentation in transparent condensed media utilized Gaussian or Gaussian-like laser pulses with durations ranging from tens of femtoseconds to several nanoseconds. Temporal pulse shaping, an approach that has proven to be very powerful in various fields of science and technology such as optical lithography [7], microscopy [8], and chemistry [9], remains largely unexplored in the context of femtosecond laser filamentation. The application of linearly chirped pulses as a means of delaying the onset of filamentation in a dispersive medium has been demonstrated [10], but the use of more complex temporal pulse waveforms in filamentation studies has yet to be adequately studied and may turn out to be a fruitful direction for future research.

One type of waveform that may be particularly interesting in the context of filamentation is the Airy pulse. The electric-field envelope of this waveform is described in terms of a truncated or apodized Airy function of time. Airy pulses are temporal analogs of Airy beams [11]. As Airy beams resist diffraction and self-bend upon propagation in free space, Airy pulses resist dispersion and their dominant intensity features accelerate temporally. Furthermore, Airy waveforms, both spatial and temporal, regenerate their dominant intensity features should those features be selectively absorbed or distorted. Since filamentation of ultrashort laser pulses in condensed media involves temporal pulse splitting as the dominant stabilization mechanism, the self-healing property of the Airy waveform may result in an even more rich and complex propagation scenario compared to that in filaments generated by Gaussian or Gaussian-like pulses.

In practice, Airy pulses are generated by applying a cubic spectral phase to the spectrum of Gaussian pulses. Depending on the sign of the cubic phase applied, the dominant intensity peak of the generated Airy waveform propagates either in front of its oscillatory tail (positive cubic phase) or behind the tail (negative cubic phase).

Temporal Airy waveforms have recently been studied in the context of their use for the construction of linear spatiotemporal light bullets [12,13]. Results on supercontinuum generation in a microstructured fiber with Airy pulses, where the self-healing ability of these temporal waveforms resulted in the generation of distinct spectral features, have also been recently reported [14].

In the present paper, we report experiments and numerical simulations on filamentation of intense femtosecond Airy

\*ppolynkin@optics.arizona.edu

waveforms in a transparent condensed medium (water). Direct measurements of the pulse evolution in this case are challenging, because the very high level of optical intensity in the filamentation zone ( $\sim 10^{13}$  W/cm<sup>2</sup>) precludes straightforward beam sampling along the propagation path. To study pulse evolution experimentally, we employ an indirect approach that relies on the analysis of the angularly resolved spectrum (or  $k$ - $\omega$  spectrum) of the forward-propagating supercontinuum emission that is generated along the filament [15,16]. Our results show that this analysis is quite sensitive to changes in the velocities of the temporal features generated upon propagation of the pulse. Our numerical simulations reproduce the experimentally measured velocities of the generated subpulses, under various conditions, without using any fitting parameters. The excellent agreement between our experimental results and numerical simulations demonstrates that this approach is capable of yielding quantitative information about propagation dynamics of sophisticated ultraintense pulse waveforms.

As mentioned above, the splitting of the ultraintense laser pulse into subpulses constitutes the natural mechanism that arrests the self-focusing beam collapse to a singularity in a transparent condensed medium. The supercontinuum radiation that is generated along the propagation path is emitted, in the forward direction, in the form of colored rings, with the particular relation between the ring color and the emission angle relative to the propagation axis. This relationship can be understood with the help of the so-called effective three-wave mixing (ETWM) picture [16]. The ETWM argument is based on the fulfillment of phase matching for the linear scattering of the continuously generated weak supercontinuum radiation on a transient “material wave.” The latter results from the instantaneous nonlinear polarization response following the two intense subpulses generated through the pulse-splitting event. The phase-matching condition governing the direction of propagation of various frequency components of the scattered supercontinuum, for a particular generated subpulse, reads

$$k_z(\omega_0, 0) - k_z(\omega, k_\perp) + \frac{\omega - \omega_0}{V_p} = 0, \quad (1)$$

where  $k_z$  and  $k_\perp$  are the longitudinal and transverse wave numbers, respectively,  $\omega_0$  is the angular frequency corresponding to the central wavelength of the incident laser pulse, and  $\omega$  is the variable that indexes the angular frequency of the scattered supercontinuum.  $V_p$  stands for the group velocity of the generated subpulse. Generally, both the subpulse velocity and its amplitude evolve upon propagation. The dominant contribution to the  $k$ - $\omega$  spectral map, from a particular generated subpulse, results from the propagation interval through which the amplitude of the subpulse is at or near a maximum. Accordingly, the value of  $V_p$  used in the phase-matching condition (1) should correspond to the sub-pulse velocity at the point of its maximum amplitude.

Experimentally, one measures the two-dimensional far-field spectra in the coordinates of the optical wavelength and  $\theta$ , the emission angle relative to the propagation axis. The relationship between  $\theta$  and  $k_\perp$  is as follows:

$$\theta = \tan^{-1} \left( \frac{k_\perp}{k_z} \right). \quad (2)$$

Note that although the propagation dynamics for a particular input pulse waveform can be excessively complex and the velocities of the generated subpulses can be, in general, arbitrary, the phase-matching condition, (1), contains only the velocity of the generated subpulse, at the point of its maximum amplitude, and the linear dispersion relation of the medium. The latter enters through the (assumed to be known) dependence of the wave number on the angular frequency.

The generation of each subpulse results in the population of a set of lines or branches on the  $k$ - $\omega$  spectral map, in accordance with condition (1) with the corresponding velocity  $V_p$  for that particular subpulse. For the case of a normally dispersive medium, such as water at a laser wavelength of about 800 nm, the branches have characteristic X shapes, and their extent is related to the propagation distance through which the corresponding subpulses survive before dissipating [16–18]. The feature corresponding to a particular subpulse consists of two disconnected lines. The point on the  $k$ - $\omega$  spectral map with coordinates  $(\omega_0, k_\perp = 0)$  corresponds to the on-axis emission at the center frequency of the incoming pulse. That point is a trivial solution of Eq. (1). For the trailing subpulse produced through a particular pulse split, the branch that contains that trivial point extends into the longer wavelength range relative to the central wavelength of the incoming pulse, while the branch corresponding to the leading subpulse that contains the trivial solution point extends into the shorter wavelength range.

The experimental setup that we use to record  $k$ - $\omega$  spectra produced through filamentation of temporal Airy pulses in water is essentially identical to that used previously in the experiments on self-focusing of spatial self-bending Airy beams [19]. To generate femtosecond temporal Airy waveforms, we use a commercial acousto-optic pulse shaper system (Dazzler by Fastlite) that is capable of imposing up to  $\pm 120\,000$  fs<sup>3</sup> of cubic spectral phase modulation onto Gaussian pulses produced by a Ti:sapphire regenerative amplifier operating at 10 pulses per second. The output spectrum of the laser is 30 nm-wide and centered at 800 nm. In the setup, the pulse shaper is placed before the pulse compressor stage of the laser system, in order not to exceed the damage threshold of the acousto-optic modulator crystal ( $\sim 100$  MW/cm<sup>2</sup>). Measurements of the generated waveforms with a femtosecond FROG system showed an excellent fidelity of the Airy pulse shapes, which were quantitatively consistent with the optical bandwidth of the pulses and with the magnitude of the applied cubic spectral phase.

The generated femtosecond Airy pulses have a nearly ideal Gaussian spatial beam profile with a beam diameter of about 5 mm. This beam is focused with a lens into a 6.5-cm-long cuvette containing pure water. The focal length of the focusing lens used is 25 cm, and the linear focal plane of the lens is positioned at a 1.5-cm distance from the entrance into the water cuvette. Over the 1.5-cm propagation distance in the water towards the focal plane, the contribution to the cubic spectral phase from the third-order dispersion of water is about 400 fs<sup>3</sup>, which is negligible in comparison with the values of the cubic spectral phase imposed by the pulse shaper. Single-shot angularly resolved spectra of the generated forward-propagating supercontinuum radiation are

recorded using an imaging spectrometer setup in the standard configuration for this application [19].

The measured  $k$ - $\omega$  spectra are numerically simulated using our standard femtosecond propagator code based on the unidirectional pulse propagation equation (UPPE) [16,20]. Our model accounts for the linear dispersion and for the instantaneous Kerr nonlinear response of the medium, as well as for multiphoton absorption and plasma effects. The value for the nonlinear Kerr refractive index  $n_2$  that we use corresponds to the critical power for self-focusing of 3.9 MW [21].

Note that if the measured and numerically simulated  $k$ - $\omega$  spectra are directly compared to each other on a linear scale, one should not expect a good quantitative agreement between experiments and simulations, because of the highly nonlinear nature of the pulse propagation problem involved and the very strong dependence of the generated spectra on the input power and duration of the laser pulse [22]. On the other hand, as we show, the morphology of the  $k$ - $\omega$  spectral maps, i.e., the placements and inclinations of the dominant features on these maps, is very well reproduced by numerical simulations, even though the feature placement is quite sensitive to variations in the velocities of the subpulses generated upon propagation. Since we are not interested in the quantitative comparison between the measured and the numerically simulated spectra, but only in the comparison between the morphologies of various branches on the spectral maps, in what follows, the numerically simulated spectra are shown on a log scale, while the spectra that are experimentally recorded are naturally shown on a linear scale. Presenting numerical data on a log scale allows for the generated branches on the  $k$ - $\omega$  spectral maps to stand out more clearly.

Our experiment-theory comparison is done according to the following procedure: The  $k$ - $\omega$  spectral map, for particular pulse shape, power, and focusing conditions, is experimentally recorded for a single laser shot. The pulse propagation, under the same experimental conditions, is numerically simulated using our propagator code. The simulation outputs the entire history of the pulse evolution upon propagation, which, of course, cannot be directly matched to the experiment. The simulation also produces the  $k$ - $\omega$  spectral map of the generated supercontinuum emission, which is compared to the map experimentally recorded. Further, by following the temporal pulse evolution upon propagation that is available from the simulation, various pulse-splitting events are identified, and the velocities of the generated subpulses, near the points of their maximum intensity, are calculated based on the simulation. The phase-matching conditions, (1), with those values of the subpulse velocities are plotted on top of both numerically simulated and experimentally measured  $k$ - $\omega$  spectral maps. It is expected that the fitting with the phase-matching condition, (1), will match the numerically simulated branches on the  $k$ - $\omega$  spectral maps very well, as has been previously demonstrated for the case of femtosecond Gaussian input pulses [16]. However, whether these fits can be applied directly, i.e., without any adjustments, to the experimentally measured spectra, is not *a priori* clear. If the fitting procedure described above is found to yield a robust quantitative agreement with experiments, the procedure could, in principle, be inverted. By fitting the branches of the experimentally recorded  $k$ - $\omega$  spectra, one could deduce the number and velocities of the

subpulses generated upon propagation, without performing a numerical simulation. This approach may be applied for a partial reconstruction of the pulse propagation scenarios in cases where the exact parameters of the experimental setup are not precisely known, making numerical simulations unfeasible.

In order to benchmark the procedure described above, we first apply it to the extensively investigated case of filamentation of a femtosecond Gaussian pulse. As we found experimentally, in our focusing geometry and with a 35-fs input pulse duration, white-light generation in the forward direction becomes observable once the input pulse energy exceeds 0.8  $\mu$ J. The onset of white-light generation is commonly associated with the self-focusing collapse of the beam. The corresponding estimated peak power at that point is 23 MW, which is about 6 times the critical power for self-focusing with a large-diameter collimated beam at infinity [21].

When the input pulse energy is increased to 1.0  $\mu$ J, the appearance of the experimentally observed  $k$ - $\omega$  spectrum stabilizes and develops straightforwardly identifiable X-shaped branches. Numerical simulation of this case reveals that the propagation of the pulse in the water cell involves two consecutive pulse-splitting events, at distances of 2.3 and 2.5 cm from the entrance into the cell. Each pulse split produces a pair of subpulses, one of which is advancing ahead of the incident pulse and the other trailing behind it. The subpulses survive for little over 0.1 mm of propagation. Upon examination of the propagation history generated by the numerical simulation, we find that the group velocities of the generated subpulses, at the points of their maximum amplitude, are  $V_{\text{lead}}^{(1)} = (1 + 0.0034)c/n_g$  and  $V_{\text{trail}}^{(1)} = (1 - 0.0083)c/n_g$  for the first splitting event and  $V_{\text{lead}}^{(2)} = (1 + 0.0068)c/n_g$  and  $V_{\text{trail}}^{(2)} = (1 - 0.0140)c/n_g$  for the second splitting event. Above,  $c$  is the speed of light in vacuum and  $n_g = 1.3434$  is the linear group refractive index of water at an 800-nm wavelength.

The phase-matching conditions, (1), for the two pairs of subpulses resulting from the splitting events are plotted in Fig. 1 by solid black lines. Evidently, the X-shaped branches on the spectral map are fit well by these phase-matching curves. As we mentioned above, the generation of each

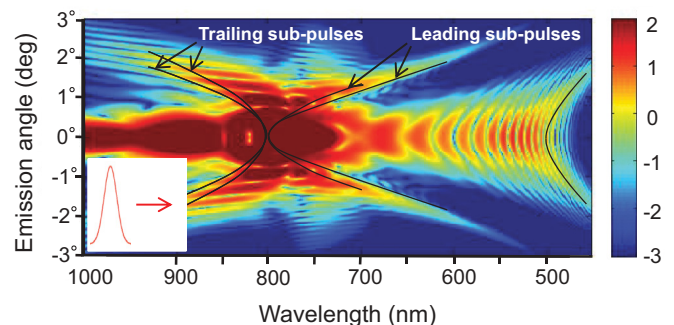


FIG. 1. (Color online) Numerically simulated  $k$ - $\omega$  spectrum generated through filamentation of a 35-fs-long Gaussian pulse with a 1- $\mu$ J pulse energy, under the experimental conditions described in the text. Data are shown on a log scale. The pulse propagation dynamics involves two pulse-splitting events. Solid black lines are drawn according to the phase-matching condition, (1), for the two generated pairs of subpulses.

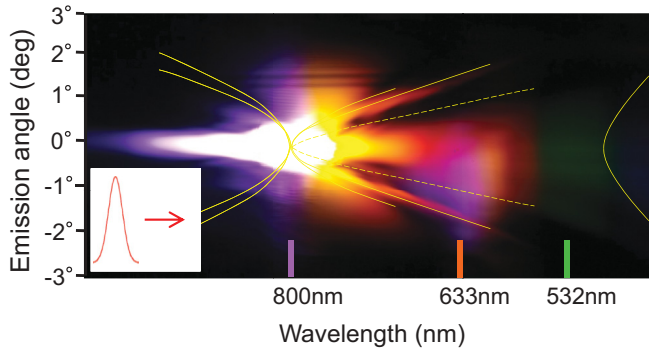


FIG. 2. (Color online) Experimentally observed  $k$ - $\omega$  spectrum for the case corresponding to the simulation shown in Fig. 1. Solid lines are exact replicas of the fitting curves reproduced here from the numerical simulation in Fig. 1 without any adjustments. The dashed line shows the fit according to Eq. (1), in which the velocity of the leading subpulse is set to  $(1 + 0.0010)c/n_g$ , which is different from the correct velocities of both leading subpulses generated upon propagation ( $c$  is the speed of light in vacuum and  $n_g$  is the linear group refractive index of water). The latter fit is clearly off the experimentally recorded branches corresponding to the two leading subpulses generated in this case.

subpulse results in the population of two disconnected lines in the  $k$ - $\omega$  spectral map, one of which contains the trivial solution point ( $\omega_0, k_{\perp} = 0$ ). Only branches containing the trivial solution point are shown in the figure. The other branches are generally outside the spectral window shown, except for the short-wavelength branch corresponding to one of the trailing subpulses.

In Fig. 2, we show the  $k$ - $\omega$  spectrum measured under the same experimental conditions as used in the simulation shown in Fig. 1. The qualitative agreement in the appearance of the measured and simulated spectra is immediately evident. Furthermore, the phase-matching curves for the two pulse-splitting events, directly replicated from the numerical fitting of the spectrum shown in Fig. 1, line up nearly perfectly with the X-shaped branches in the experimental plot.

To demonstrate the sensitivity of the feature placement in the spectral maps to variations in the group velocity of the subpulses, we show, in the same plot, the phase-matching curve corresponding to the subpulse advancing with a group velocity equal to  $(1 + 0.0010)c/n_g$ , which is different from the correct velocities of the two leading subpulses generated upon propagation in this case. The resulting fitting curve is shown in Fig. 2 by the dashed line. That fit noticeably disagrees with the experimental data. This example shows that the fitting procedure is sensitive to the changes in the group velocities of the generated subpulses and that these velocities can, in principle, be extracted from the experimentally measured  $k$ - $\omega$  spectra. The accuracy of the reconstruction of the subpulse velocities, relative to the linear group velocity in water, can be roughly estimated as  $\sim 20\%$ .

After demonstrating the excellent agreement between experiments and numerical simulations for the case of an input Gaussian pulse, we move on to the more complex case of accelerating Airy waveforms. These waveforms are synthesized, both experimentally and numerically, by imposing cubic spectral phases of different signs onto the optical spectrum of

an input Gaussian pulse. The pulse energy is adjusted so that the peak power of the dominant intensity feature of the Airy pulse matches that of the input Gaussian pulse used earlier. In our case, the peak power matching, for the cases of a cubic spectral phase of  $\pm 120\,000\text{ fs}^3$ , is achieved by increasing the pulse energy from 1 to  $1.6\ \mu\text{J}$ .

Note that, out of the two main features of an Airy waveform, self-healing and free acceleration, the first feature is not expected to be operative and produce a significant effect under our experimental conditions. The self-healing of distorted or attenuated intensity features relies on the temporal reshaping of the waveform via chromatic dispersion. Accordingly, this effect will reveal itself in the characteristic propagation distances of the order of the dispersion length in the medium, at a given pulse duration. In our case, the dispersion length corresponding to the  $\sim 70$ -fs intensity FWHM of the main peak of the Airy pulse is about 7 cm, which is much longer than the Rayleigh range of the laser beam in our focusing geometry. On the other hand, as our results show, the accelerating feature of the Airy waveform will play a significant role both in the pulse propagation dynamics and in the resulting morphology of the generated  $k$ - $\omega$  spectra.

Indeed, numerical simulations of the propagation of Airy waveforms with  $\pm 120\,000\text{ fs}^3$  of cubic spectral phase in water, under our experimental conditions, reveal that the pulse propagation dynamics for cases of the same magnitude but opposite sign of the cubic spectral phase are markedly different. In both cases, the main peak of the waveform splits upon propagation three times, while the secondary peak of the waveform undergoes a single splitting. The splits occur in the range of propagation distances from 2.2 mm to 2.6 cm from the entrance to the water cell. Due to the opposite directions of temporal accelerations of Airy pulses with opposite signs of cubic spectral phase, the velocities of the intensity features that undergo splitting, as well as the velocities of the resulting subpulses, are different, which translates into a noticeable difference in the morphology of the generated  $k$ - $\omega$  spectral maps.

For example, for a positive cubic spectral phase, in which case the dominant intensity feature of the pulse propagates in front of the oscillatory pulse tail, the three splits of the main intensity feature of the waveform result in the population of nearly overlapping branches in the  $k$ - $\omega$  spectral map. Fitting curves based on the phase-matching condition, (1), with the group velocities of the subpulses extracted from the numerical simulation are shown, by solid lines, in the top part of Fig. 3. The dashed line in the same figure shows the phase-matching condition for the subpulse produced through the only split of the secondary intensity feature of the pulse. That curve is very close to the curves for the three consecutive splits of the dominant intensity feature.

The simulated  $k$ - $\omega$  spectrum for the case of a negative cubic spectral phase, corresponding to the dominant peak of the waveform propagating behind its oscillatory tail, is shown in the bottom part of Fig. 3. As in the previous case, the X-shaped arms produced by the first two splits of the dominant intensity feature of the pulse, as well as by the split of its secondary feature, are nearly overlapping. However, the third split of the dominant feature produces a standout arm shown by the dashed line. In that case, the trailing subpulse moves with

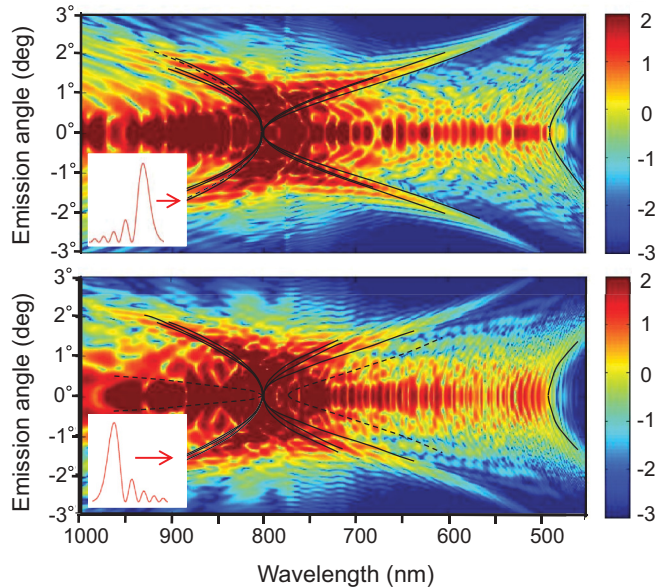


FIG. 3. (Color online) Numerically simulated  $k$ - $\omega$  spectra for cases of Airy pulses with  $1.6 \mu\text{J}$  of pulse energy and with a positive (top) and a negative (bottom) cubic spectral phase of  $120\,000 \text{ fs}^3$ . Insets: The corresponding orientations of the waveforms. Spectra are plotted on a log scale. For the positive phase case, the phase-matching curves for the three splits of the dominant intensity feature of the waveform are shown by solid lines. The dashed line shows the phase-matching curve for the split of the secondary feature of the pulse. For the negative phase case, the solid lines show the phase-matching curves for the first two splits of the dominant intensity feature of the pulse and for the only split of the secondary feature. The dashed lines show the phase-matching curves for the third split of the main intensity feature.

a group velocity of  $(1 - 0.0010)c/n_g$ , which is very close to the linear group velocity in water. Both branches of the phase-matching curve, (1), for the trailing subpulse produced in that splitting event are visible in the spectrum, as they both fit into the measured spectral window. In the simulation plot shown in the bottom part of Fig. 3, these branches are shown by dashed lines.

The experimentally measured  $k$ - $\omega$  spectra for cases corresponding to the simulations shown in Fig. 3 are shown in Fig. 4. The qualitative match between the numerical and the experimental spectral patterns is evident, for the cases of both positive and negative cubic spectral phases used to generate these Airy waveforms. In the case of a positive cubic spectral phase, one single extended diagonal arm is present on the blue (right) side of the  $k$ - $\omega$  spectral map. In the case of a negative cubic phase, two distinct diagonal arms on the blue (right)

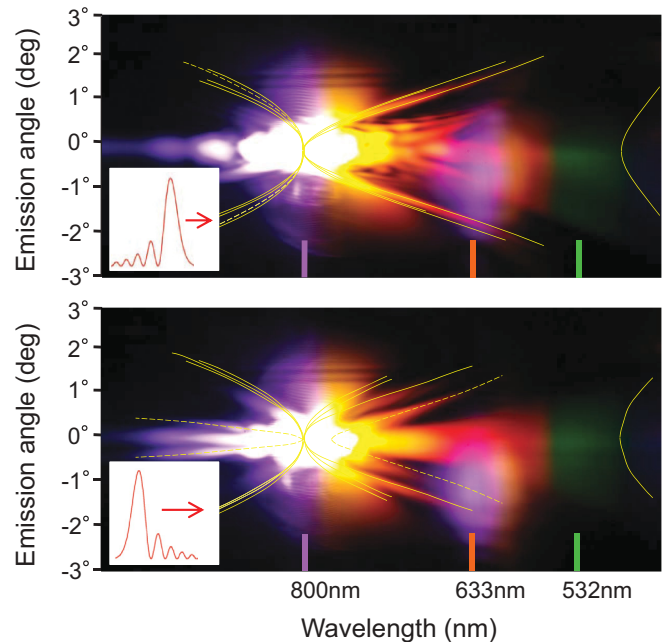


FIG. 4. (Color online) Experimentally observed  $k$ - $\omega$  spectra for the cases of Airy pulses corresponding to the numerical simulations shown in Fig. 3. The top figure corresponds to a positive, and the bottom figure to a negative, cubic spectral phase of  $120\,000 \text{ fs}^3$ . Lines are exact replicas of the corresponding fitting curves from the numerical simulation plots shown in Fig. 3.

side of spectrum, as well as an extended arm close to the horizontal axis on the red (left) side, are evident. Numerical simulations reveal the origin of these features, as discussed above. The phase-matching curves, directly replicated from the simulation plots in Fig. 3 onto the experimental plots in Fig. 4, show an excellent agreement with the placements of the experimentally recorded spectral features.

In conclusion, we have analyzed, both experimentally and numerically, the nonlinear propagation of femtosecond accelerating Airy waveforms in water. We have shown that analysis of the morphological features in the  $k$ - $\omega$  spectral maps of forward-propagating supercontinuum emission provides quantitative clues on the complex evolution of these sophisticated pulse waveforms in the highly nonlinear propagation regime.

This work was supported by The United States Air Force Office of Scientific Research under Programs FA9550-10-1-0237 and FA9550-10-1-0561. Craig Ament acknowledges support by the Graduate Scholarship from the Directed Energy Professional Society.

- [1] A. Couairon and A. Mysyrowicz, *Phys. Rep.* **441**, 47 (2007).  
 [2] J. Kasparian and J. P. Wolf, *Opt. Express* **16**, 466 (2008).  
 [3] S. L. Chin, *Femtosecond Laser Filamentation* (Springer, New York, 2010).

- [4] V. Loriot, P. Bejot, W. Ettoumi, Y. Petit, J. Kasparian, S. Henin, E. Hertz, B. Lavorel, O. Faucher, and J.-P. Wolf, *Laser Phys.* **21**, 1319 (2011).  
 [5] J. K. Ranka, R. W. Schirmer, and A. L. Gaeta, *Phys. Rev. Lett.* **77**, 3783 (1996).

- [6] A. Couairon, E. Gaizauskas, D. Faccio, A. Dubietis, and P. Di Trapani, *Phys. Rev. E* **73**, 016608 (2006).
- [7] A. N. Boto, P. Kok, D. S. Abrams, S. L. Braunstein, C. P. Williams, and J. P. Dowling, *Phys. Rev. Lett.* **85**, 2733 (2000).
- [8] J. P. Ogilvie, D. Debarre, X. Solinas, J.-L. Martin, E. Beaurepaire, and M. Joffre, *Opt. Express* **12**, 759 (2006).
- [9] I. Pastirk, E. J. Brown, Q. Zhang, and M. Dantus, *J. Chem. Phys.* **108**, 4375 (1998).
- [10] G. Mechain, C. D'Amico, Y.-B. Andre, S. Tzortzakis, M. Franco, B. Prade, A. Mysyrowicz, A. Couairon, E. Salmon, and R. Sauerbrey, *Opt. Commun.* **247**, 171 (2005).
- [11] G. A. Siviloglou, J. Broky, A. Dogariu, and D. N. Christodoulides, *Phys. Rev. Lett.* **99**, 213901 (2007).
- [12] A. Chong, W. H. Renninger, D. N. Christodoulides, and F. W. Wise, *Nature Photon.* **4**, 103 (2010).
- [13] D. Abdollahpour, S. Suntsov, D. G. Papazoglou, and S. Tzortzakis, *Phys. Rev. Lett.* **105**, 253901 (2010).
- [14] C. Ament, P. Polynkin, and J. V. Moloney, *Phys. Rev. Lett.* **107**, 243901 (2011).
- [15] D. Faccio, P. Di Trapani, S. Minardi, A. Bramati, F. Bragheri, C. Liberale, V. Degiorgio, A. Dubietis, and A. Matijosius, *J. Opt. Soc. Am. B* **22**, 862 (2005).
- [16] M. Kolesik and J. V. Moloney, *Opt. Express* **16**, 2971 (2008).
- [17] D. Faccio, A. Averici, A. Couairon, M. Kolesik, J. V. Moloney, A. Dubietis, G. Tamosauskas, P. Polesana, A. Piskarkas, and P. Di Trapani, *Opt. Express* **15**, 13077 (2007).
- [18] D. Faccio, M. A. Porras, A. Dubietis, F. Bragheri, A. Couairon, and P. Di Trapani, *Phys. Rev. Lett.* **96**, 193901 (2006).
- [19] P. Polynkin, M. Kolesik, and J. V. Moloney, *Phys. Rev. Lett.* **103**, 123902 (2009).
- [20] M. Kolesik, J. V. Moloney, and M. Mlejnek, *Phys. Rev. Lett.* **89**, 283902 (2002).
- [21] Z. W. Wilkes, S. Varma, Y. H. Chen, H. M. Milchberg, T. G. Jones, and A. Ting, *Appl. Phys. Lett.* **94**, 211102 (2009).
- [22] B. Shim, S. E. Schrauth, A. L. Gaeta, M. Klein, and G. Fibich, *Phys. Rev. Lett.* **108**, 043902 (2012).